Corrosion at the carbon steel- clay compact interface at 90°C: insight into short- and long-term corrosion aspects

M. L. Schlegel[1], F. Martin[2], M. Fenart[2], C. Blanc[1], J. Varlet[1], E. Foy[3], D. Prêt[4], N. Trcera[5]

1 Den – Service d'Etudes Analytiques et de Réactivité des Surfaces (SEARS), CEA, Université Paris-Saclay, F-91191 Gif sur Yvette, France

2 Den – Service de Corrosion et du Comportement des Matériaux dans leurs Environnements (SCCME), CEA, Université Paris-Saclay, F-91191 Gif sur Yvette, France

3 LAPA-IRAMAT, NIMBE, CEA, CNRS, Université Paris Saclay, CEA Saclay, F-91191 Gif-sur-Yvette, France

4 UFR Sciences fondamentales et appliquées, Université de Poitiers, F-86073 Poitiers, France

5 LUCIA Beamline, Synchrotron SOLEIL, F-91190 Saint-Aubin, France

Abstract

Rods of low alloy carbon steel were corroded under anoxic conditions in compact clay at 90°C. Gravimetrically-assessed corrosion damage equalled 8.5 µm at 7 months, then slowly increased to 29.5 µm at 76 months. The corrosion damage was heterogeneous at 7 months, and two distinct aspects coexisted: steel was replaced by (Fe,Si,O) corrosion products in some areas, and by Si-poor hydroxide and covered by akaganeite (FeO(OH,Cl)) in others, indicating corrosion in suboxic conditions. A magnetite fringe contacted the steel surface. For greater reaction times, akaganeite disappeared, and only (Fe,Si,O) corrosion products containing Fe sulfide and chukanovite were detected.

Keywords

Carbon steel (A) ; Clay (A) ; SEM (B) ; XRD (B) ; Raman spectroscopy (B)

1 Introduction

Due to its low cost, durability, and advantageous mechanical properties, low-alloy carbon steel (C-steel) has been widely used in the oil, gas, geothermal and drinking water industries. Based on the extensive knowledge gained from these applications, it has also been investigated as a material for the production of long-term barriers surrounding High-Level nuclear Waste (HLW) in deep geologic repositories. For example, the French design relies on confining HLW glass and its stainless steel containers within C-steel overpacks inserted in C-steel cased tunnels drilled within the host rock [1, 2]. The potential host rock, Callovo-Oxfordian (COx) claystone, has been selected because of its good confinement properties and low permeability. The overpacks should protect the stainless steel containers, and *de facto* the nuclear glass, during the thermal phase ($T \geq 50°C$). The casing (also made of C-steel) should guarantee the reversibility of the waste disposal over the operation period of the repository (more than one century). In early designs, contact between clay and casing C-steel was expected, resulting in corrosion in a compact C-steel-clay interface and ultimately degradation of the casing mechanical properties. After sealing of the repository, corrosion is first expected to occur in the presence of oxygen. Next, rapid consumption of O_2 by corrosion and biogenic processes will lead to anoxic conditions [3], and radioactive decay will increase the temperature up to 90°C at the overpack outer surface. Under this combination of contact geometry and physico-chemical conditions, general corrosion was expected to predominate for C-steel [4, 5]. However, recent work has demonstrated that pitting corrosion also could occur, though with limited effect as pits would remain metastable and tend to close up [5]. Hence, a better understanding of C-steel corrosion in contact with clay was deemed necessary to predict the long-term behaviour of C-steel envelopes in the repository.

Insight into the interaction of C-steel with complex environmental materials can be obtained from a variety of integrated experiments and *in situ* observations. For example, the study of steel archaeological artefacts embedded in water-saturated anoxic soils provided a unique insight into corrosion processes operating at ambient temperature [6-12]. Microstructural characterisation of the corrosion interfaces revealed their structural layering and the prevalence of Fe oxide and (hydroxy)carbonate. Yet, investigation of these corrosion systems operating at (near)-ambient temperature provides only limited insight into the effect of temperature on e.g. corrosion rate (CR), precipitation rates of solids, and the nature

of corrosion products (CP) under repository representative conditions. Integrated experiments with pure ferrite in contact with clay at temperatures about 90 °C were designed to address these issues [13-21]. These investigations were performed for up to two years and revealed the formation of distinct corrosion layers essentially made of magnetite (Fe_3O_4) close to the metal, Fe silicate, and siderite ($FeCO_3$) [18, 19, 22]. However, results obtained on pure ferrite cannot be readily applied to cementite-containing C-steel. Actually, for pure ferrite, both cathodic and anodic reactions occur at the same interfacial location (though not necessarily at the same time), resulting in the formation of a protective barrier layer made of Fe oxide [23-26]. In contrast, for C-steel, the presence of cementite, which exhibits a lower overpotential, will favour localized galvanic coupling, leading somehow to substantially greater corrosion kinetics [27, 28]. In fact, these differences are readily observed in several experiments comparing the behaviour of pure iron and C-steel under similar solution conditions [29]. Thus, a thorough investigation of CR and CP at the C-steel-clay interface, possibly over periods of several years, is warranted.

The present study investigates the damage rates and interface evolution resulting from over six years of C-steel corrosion in clay rock at 90°C under anoxic, water-saturated conditions. These experiments extend and complete previous observations made on shorter time scales [30]. Corrosion damage was quantified by gravimetric analysis, or by direct estimates on sample sections; both methods suggested a short-to-long term transition in CR. The nature and distribution of CP were identified, their evolution with time confirming a change in corrosion control from suboxic to anoxic carbonated clay conditions.

2 Materials and methods

2.1 Starting materials

All steel samples were made of A37 C-steel, with a composition (wt %) of 0.12C–0.62Mn–0.22Si–0.12P–0.12S–0.008Al–0.03Cr–0.04Cu–0.02Ni – balance Fe. The C-steel, taken from a cold-rolled bar, is essentially ferritic, with about 8% of pearlite textured in bands aligned along the rolling direction. Clay was cored from the COx formation in the Meuse-Haute Marne Underground Laboratory (Bure, France). It essentially contains calcite ($CaCO_3$; 30 wt.%), quartz (SiO_2; 30 wt.%), interstratified illite-smectite (~35 wt. %), and minor amounts of pyrite (FeS_2), siderite, and feldspars ($CaAl_2Si_2O_8$-$(Na,K)AlSi_3O_8$) [31, 32].

Synthetic clay porewater was prepared fresh by dissolving salts in high-purity water. The porewater composition (Table 1) is representative of the COx formation [33, 34]

2.2 Experimental setup

Three steel sample geometries were implemented (Figure 1a). Type 1 was a massive C-steel rod (diameter 10 mm, length 30 mm) and was devoted to the study of the massive C- steel-clay interfaces. Type 2 was made using two short rods of 14 and 15 mm length, respectively, separated by a PTFE disk (9 mm diameter, 1 mm thickness), to investigate corrosion in a pseudo-crack. Type 3 was made using an A37 tube sealed with two disks (total length 30 mm, outer diameter 16 mm), pierced with six holes and containing a small A37 rod (diameter 8 mm, length 20 mm) insulated from the external tube by polytetrafluoroethylene (PTFE) rings to avoid galvanic coupling. These specimens, thereafter referred to as 'microcontainers', were designed to investigate entry of clay porewater into the space between the liner/casing and the overpack. Samples were inserted in clay cylinders with clay lids, both machined from COx clay and with the cylindrical axis oriented perpendicular to the clay sedimentary plane (Figure 1b,c). These setups were then inserted into high-pressure cells with welded lids, and saturated with synthetic clay porewater. The high-pressure cells were immersed in an oil bath heated at 90 °C, with the axes of the clay cylinders (and of the specimens) oriented horizontally (Figure 1d). The synthetic clay porewater was pushed from a reservoir through the clay cylinders by applying an upstream overpressure ranging from 12 to 27 bars (He). This overpressure generated a slow but steady renewal of the porewater around the specimens. The pressure cells were fed in parallel from the reservoir to guarantee identical input conditions. Vessels with a low internal pressure (initially ~1 bar) were placed downstream to collect the flux water and possible reaction gases (e.g. hydrogen). At given times, one cell from each of the three types of samples was removed and dismantled. Upon dismantling the first samples, a weak odour of rotten eggs was noted, suggesting the presence of a limited amount of hydrogen sulfide. One sample of each type was transferred into a glove box for structural characterisation, and the others were used for gravimetric measurement of the corrosion damage, after treatment in an acid bath (to remove oxides and residual clay parts) containing corrosion inhibitors (to minimize metal dissolution). The overall uncertainty for the

106 damage values averages ± 0.6 µm. In this contribution, only the massive rods were investigated (Table 2).
107 Results for the specimens with pseudo-cracks and the microcontainers will be given in a sequel.

108 *2.3 Sample preparation for microcharacterisation*

109 For microstructural characterisation, C-steel samples and adhering clay were embedded with epoxy
110 resin. The massive rods (Type 1) were cut perpendicular to the rod axis, fitted into 25 mm moulds, and
111 then impregnated with epoxy resin (Epofix, Struers). Impregnated sections were polished using silicon
112 carbide (SiC) papers, and diamond pastes in ethanol, down to a final roughness of 1 µm. Preparation was
113 performed in a glove box under a N_2 atmosphere to minimize sample oxidation.

114 For micro X-Ray Diffraction (µXRD), the polished surfaces were thinned to 100 µm and mounted on
115 a sample holder under anoxic conditions, as described elsewhere [35, 36].

116 *2.4 Microcharacterisation techniques*

117 For optical imaging and micro Raman spectroscopy (µRS), sample sections were kept in airtight boxes
118 with a 1 mm thick glass window. An Olympus BX51M microscope equipped with a CCD camera (Sony
119 Exwave HAD) was used to image the corrosion interface, and the images were stitched using the analySIS
120 software. Micro Raman spectra were recorded on microspectrometers (Renishaw Invia for the first
121 samples, and later LabRam HR800) with 50× long-range objectives, laser beams with wavelengths of 532
122 or 785 nm and power outputs of ~500 µW. Spectra were accumulated to obtain a correct signal-to-noise
123 ratio.

124 For scanning electron microscopy (SEM), samples were coated with a thin carbon layer, and then
125 transferred quickly into the microscope. The microscope (JEOL JSM7000-F with a field emission gun)
126 was operated at 10 kV and 1.6-2 nA. Images were obtained in Backscattered Electron (BSE) mode, and
127 Energy-Dispersive X-ray (EDX) spectra were recorded on Points of Interest (PI) using a silicon-drift
128 detector (Bruker XFlash 5010) and processed with the Esprit system (Bruker). A top hat background
129 removal and a $\phi\rho z$ algorithm were sequentially used to correct the EDX spectra for absorption and
130 secondary fluorescence. Quantifications are given in atomic percent (at.%), and are rounded to two
131 significant digits in the text. Maps of raw counts for selected chemical elements were recorded by sample

continuous scanning and adding the EDX signal on each pixel. The dwell time per pixel per frame was ~256 µs, and total counting times were 2 to 16 h. One map was collected at a higher probe current (10 nA) and subject to extensive quantitative analysis, as detailed in a companion paper (Prêt *et al.*, in preparation).

The µXRD data were recorded in transmission mode, with the polished surface oriented vertically and perpendicularly to the incident X-ray beam. X-rays from a rotating anode source (Mo Kα radiation) were focused to 30×50 μm^2 (vertical×horizontal). Diffraction patterns were collected with a 2D Image plate detector (GE Healthcare) and integrated with the FIT2D software [37].

Micro X-Ray Fluorescence (µXRF) and micro X-ray Absorption Fine Structure (µXAFS) spectra were recorded on the LUCIA beamline [38] of the SOLEIL synchrotron (Saint Aubin, France). The synchrotron ring was operated at 2.75 GeV and 400 mA. X-rays were obtained from an undulator source, and X-ray energies at the Si and S K-edges were selected using an InSb(111) double crystal monochromator. The beam was focused down to 3×4 μm^2 and 10×10 μm^2 (vertical×horizontal) at the S and Si K-edges, respectively, by a Kirkpatrick-Baez setup. The samples were glued on a copper sample holder in the glove box, kept in an anoxic container, and rapidly transferred (< 5 min) from the container to the beamline experimental chamber. The chamber atmosphere was then pumped to < 1 mbar, and the sample cooled to 150 K by a cooling thread bound to the cold head of a He cryostat. The normal to the sample plane was tilted horizontally by 10° off the X-ray beam, and X-ray fluorescence was recorded using a single-element silicon drift detector at 90° with respect to the incident X-ray beam. Elemental maps were collected by sample scanning with a dwell time of 1 s per pixel. µXAFS spectra were collected on PI and corrected for self-absorption [39, 40]. Minerals references were pressed into pellets for µXAFS measurements. Data reduction and analysis was performed using standard procedures and the Athena-Iffefit software [41-44].

3 Results

3.1 Gravimetric analysis

Gravimetric assessments for simultaneously sampled specimens showed some scatter (Figure 2), part of which can be attributed to the intrinsic heterogeneity in C-steel microstructure and clay. Sample damage after 7 months of reaction is significant, averaging 8.5 ± 3 µm. With increasing reaction time, the damage

158 increased at a slower rate, and after 76 months, it amounts to 29.5 ± 3 µm. It thus appears that damage of
159 the massive rods in contact with clay was quite limited, even after 76 months.

160 Evaluation of the corrosion kinetics (or damage evolution with exposure time) throughout the 76
161 months was assessed by fitting logarithmic, power or linear laws according to different prevailing
162 mechanisms. The logarithmic law did not fit the data well, and was discarded. In contrast, the power law
163 (PL) provides a reasonably good fit for damage values below 40 months, even if some discrepancy appears
164 for longer exposure times (Figure 2). The best fit was obtained using the equation:

$$Damage_{PL}(t) = 10.6 \times t^{0.49} \quad (1)$$

165 where $Damage_{PL}(t)$ (in µm) is the modeled damaged thickness (in µm) using the PL and t is the time (in
166 years). The exponent value of 0.49 suggests that the damage evolution with time is parabolic. The liner
167 law (LL) fits very well all data points, but fails to meet the origin coordinates. The best-fit is given by

$$Damage_{LL}(t) = 6.7 + 3.54 \times t \quad (2)$$

168 The LL also provides greater values for long-term damage. It may thus be used for conservative
169 extrapolations beyond the experiment duration, assuming the corrosion mechanism does not change.

170 ### *3.2 Interfacial characterisation*

171 Heterogeneous generalized corrosion was observed for all cross-sections, with hardly corroded areas
172 coexisting with local depressions (Figure 3). For the 7-months specimens, the depressions had depths of
173 usually ~10 µm, with a few values down to ~30 µm (Figure 3a-c). The maximum depth of these
174 depressions increased to 90 µm after 76 months of reaction time. These depressions were filled with CP,
175 sometimes mixed with cementite *lamellae*, confirming the CP replaced C-steel by inward growth (Figure
176 3d). Hence they correspond to a Dense Products Layer (DPL). For corrosion times over 40 months, the
177 DPL seemed to differentiate into two distinct sublayers of slightly contrasted electron density (Figure 3e,f).
178 The DPL was overlaid with an irregular and relatively thin layer (about 5 µm thick; Figure 3c,d,f), hereafter
179 referred to as Median Corrosion Layer (MCL). This MCL also contained cementite *lamellae*; the top of
180 the MCL coincided with the end of cementite *lamellae*, highlighting the Trace of the Original Steel Surface

(TOSS). Finally, particles with greater electron density (visible as brighter areas on BSE images) could be observed locally inside the clay rock close to the TOSS, forming a Transformed Matrix Layer (TML).

From the CP analysis, two distinct types of corrosion interfaces could be discriminated for the 7-months specimen. Most of the 7-months DPL was essentially made of a (Fe, Si) (hydr)oxide (Figure 4a) containing substantial amounts of Na (Table 3, PI 2-3). In some areas, this layer seemed to directly contact the C-steel, but in other areas it was separated from metal by a fringe of iron oxide (Table 3, PI 1, Figure 4b). The MCL composition is notably distinct from the DPL. In most areas, the MCL has a fair amount of Fe and Ca and is enriched in O with respect to the DPL (Table 3, PI 4-5), suggesting the formation of a Ca-rich siderite (ankerite; $(Fe,Ca)CO_3$). This composition could vary locally, as shown by the observation of some O-depleted, S-enriched areas. Although not quantified in these early characterisations, coupled (Cu,S) contributions could also be observed by EDX analysis, suggesting the formation of Cu sulfide. Finally, the clay rock close to the TOSS was somewhat mixed with (Fe, Ca)-containing material, suggesting the precipitation of ankerite (Table 3, PI 6).

In some limited areas of the interface for the 7-months specimen, a notably distinct interfacial arrangement could be observed (Figure 5a). The Si content of the DPL was notably low (1.3-1.4 at.%), and this depletion is balanced by Fe enrichment (Table 4, PI 1-2). The µRS signal of the DPL corresponds to poorly ordered $Fe^{(III)}$ (hydr)oxide (Figure 5b). The MCL was still present with an ankerite-type composition (Table 4, PI 3). In contrast, most of the clay was replaced by a massive Fe (hydr)oxide significantly enriched in Cl (up to 0.9 at.%, Table 4, PI 4-5), and identified by µRS as akaganeite (FeO(OH,Cl)) (Figure 5c). The presence of $Fe^{(III)}$ (hydr)oxides indicates that some initial stages of C-steel corrosion occurred under (sub)oxic conditions, probably due to residual oxygen in the setup. Even at trace levels, oxygen can induce the formation of pit-like corrosion areas, thus explaining the heterogeneity in surface damage [45, 46].

Compared to these 7-months sample, the corrosion interfaces from 15 to 76 months of reaction showed remarkable consistency in terms of the nature and distribution of CP (Figure 6). Firstly, akaganeite or any other Cl-containing solid were no longer observed. Next, most of the DPL appeared enriched in O (56-70 at.%) and Si (from 5 to 21 at.%) (Table 5, PI 1, 2, 5-7, 9, and 10). A magnetite fringe between the C-steel

and CP was observed only on a thin fraction of the interface (for example less than 0.2 % of the entire C18 interfacial cross-section). In addition, the DPL layer contains around 1-2 at.% of S, with end values around 0.7 and 2.5 at.%. Some Al enrichment was detected in the C09 DPL, reaching about 1 at.% (Table 5, PI 1-2), and Na was significantly present in the C12 DPL (1.2 to 1.6 at.%; Table 5, PI 5-7). The wide fluctuations in Fe/Si ratios (from 1 to 4) may be attributed to the coexistence of several Fe silicates in varying amounts, possibly also intermixed with Fe (hydroxy)carbonate (Prêt *et al.*, in preparation). Additional proof for the coexistence of two Fe-rich solid phases was provided by µRS data displaying a peak near 1070 cm^{-1}, which diagnostic of chukanovite ($Fe_2(OH)_2CO_3$), and bands near 258-260, 285, 314, and 358 cm^{-1} assigned to Fe sulfide (Figure 7). Interestingly, Fe silicate, although being the major component of the layer, had no conspicuous µRS contribution.

In an attempt to characterize the nature of the Fe silicate phase, µXAFS spectroscopy was performed on the CP within a corrosion depression of the C15 sample (Figure 8). As a preliminary step, the location of the corrosion layers was determined using µXRF spectroscopy (Figure 8a,b). Several µXAFS spectra were collected in the DPL layer (PI X1-X4) or in the nearby clay (PI X5, X6). All spectra display the main absorption "white line" (peak A) at 1847 eV typical of Si in a silicate group [47] (Figure 8c). Additional examination showed that all spectra except X5 were dissimilar to the amorphous silica or quartz references, but were rather similar to the clay references (Figure 8c). Specifically, sample spectra displayed a weak shoulder (labelled B) near 1851 eV and broad absorption bands near 1856.9-1857.2 (peak C) and 1862.8-1863.1 eV (peak D). The peak positions and amplitudes were similar to those observed for nontronite (nominally $Na_{0.3}Fe_2(Al_{0.3}Si_{3.7})O_{10}(OH)_2$) (features B, C, D at 1850.2, 1856.8 and 1863.2 eV, respectively) or montmorillonite (nominally $Na_{0.3}Al_{1.7}Mg_{0.3}(Si_4)O_{10}(OH)_2$) (1850.8, 1857.2 and 18652.9 eV, respectively) suggesting a phyllosilicate tetrahedral-octahedral-tetrahedral (TOT)-like structure. Feature B in the sample is also close to the positions observed for greenalite (nominally $Fe_3(Si_2)O_5(OH)_4$) (1850.9 eV) or chamosite (nominally $(Fe,Mg,Al)_6(Si,Al)_4O_{10}(OH)_8$) (1850.8 eV), but peak C for these references (1856.2 and 1856.4 eV, respectively) are shifted to lower values compared to the samples. Finally, the montmorillonite spectrum displays an additional shoulder near 1866.5 eV (D') which is absent in sample

spectra. Overall, this comparison suggests that Si environment in the DPL compares with Si in nontronite, yet additional contributions from minor environments are not excluded.

In addition to Si, the chemical nature of S, a DPL trace compound, was investigated by S K-edge µXAFS spectroscopy. Areas of significant S content and PI candidates were first located by µXRF mapping (Figure 9a-c). Spectra collected at these PI all display a first peak at 2470 eV, followed by a broad band near 2476 eV (Figure 9d). The first peak is intermediate in position between the peaks for S at an oxidation state of –II, as in chalcopyrite, and –I, as in pyrite (FeS_2) [48]. This suggests that the oxidation state of S for this contribution is intermediate between –II and –I. The broad band is similar in position to the band observed for chalcopyrite, suggesting that the S chemical environment would be somewhat similar to that observed in a sulfide compound. This clearly points to $S^{(-II)}$, perhaps partially oxidized. This inference was confirmed by comparison with the spectrum of S in pyrrhotite (Fe_7S_8) [49], meaning that S is present as an Fe sulfide. This result corroborates µRS observations of oxidized mackinawite in the DPL (Figure 7). A second, narrow peak could sometimes be observed near 2482 eV, but the intensity of this band quickly decreased upon X-ray irradiation. This narrow band was attributed to $S^{(VI)}$ in sulphate groups (Figure 9) [48], and its decrease in amplitude indicated that photoreduction issues were not completely resolved by the cryogenic setup. Interestingly, though, quantitative analysis performed in the companion paper hinted at the possible presence of a sulphate solid (i.e. gypsum, $CaSO_4$) in the DPL for the 76-months sample (Prêt *et al.*, in preparation).

The MCL between the DPL and clay is somewhat discontinuous, yet it can be found indifferently over areas of extended or limited corrosion. It contains Fe (~12 at.%), Ca, (~6 at.%) and Mg (up to 2.5 at.%). The O content is about 78 at.%, resulting in O/(Mg + Fe + Ca) ratio around 3-4, which is typical of (hydrated) carbonate minerals (Table 5, PI 8). This composition corresponds to ankerite, the presence of which was confirmed by µRS data showing the typical bands at 185, 286, and 1090 cm^{-1} (Figure 10). Ankerite formation in clay near the TOSS was often observed in setups operated under comparable conditions [18, 19, 21, 22]. Laterally, ankerite can be replaced by Fe sulfide or Cu sulfide (Cu maps of C6 and C15, Figure 6). The Cu/S ratio for these solids is close to 2, suggesting the formation of Cu_2S (Table 5, PI 3).

Finally, the clay in contact with the corrosion surface contains significant amounts of Si, Al, K, and Ca, as expected. Close to the interface, the clay matrix also contains Fe-rich minerals with a chemical composition corresponding to ankerite (Table 5, PI 4). In a few instances, grains of chalcopyrite were observed and identified by µRS.

In conclusion, corrosion at the C-steel-clay interfaces shows some consistent trends over the reaction time from 7 to 76 months, with the formation of a Si-rich DPL, of a MCL essentially made of ankerite and Fe or Cu sulfide, and of a TML containing ankerite and, locally, chalcopyrite. A unique feature of the samples with the shortest reaction time (7 months) is the presence of Cl-containing $Fe^{(III)}$ oxyhydroxyde (akaganeite), indicating initial suboxic corrosion. With increasing corrosion time, akaganeite disappears, the Na content in the DPL generally decreases, and the corrosion interface becomes remarkably steady in terms of structure and composition. Note that corrosion may occur next to pearlite particles, leaving cementite *lamellae* mixed with CP (e.g. Figure 6, BSE image of C12). Overall, however, the location of the areas with the greatest damage seems to be independent of the proximity of cementite *lamellae*, and is probably rather driven by the presence of C-steel defects or clay heterogeneities nucleating corrosion depressions.

3.3 Estimation of corrosion damage at the C-steel-clay interface from sample sections

Estimation of the corroded thickness of metal can be made by measuring the distance between the TOSS and the current C-steel-CP interface. Since the rod cross-section is circular, the TOSS was estimated by a circle touching the metal surface in areas of almost nonexistent corrosion. Damaged thicknesses were measured on the SEM images along *radii* oriented every 1° from the circle center (up 360 measures). The estimated thicknesses (Table 6) are generally consistent with values obtained from gravimetric analysis. The calculated large standard deviations do not result from uncertainty in thickness measurements (very liberally estimated to be ± 5 µm), but rather reflect the heterogeneity of the corrosion around the sample, as usually observed in contact with clay or soil [50].

4 Discussion

4.1 Mechanisms of corrosion at the C-steel-clay interface

The systematic investigation of the C-steel-clay interface corroded at 90°C for increasing times provides a unique insight into the evolution of the interfacial morphology and mineralogy. For the whole series of samples, corrosion is isovolumic and heterogeneous, with shallow depressions and large, hardly damaged areas. Over time, the relative proportion of significantly damaged areas increases, a clear indication of generalized corrosion. For a reaction time of seven months, corrosion results in the formation of Fe (hydr)oxide (magnetite detected by µXRD), of a (Fe,Si) (hydr)oxide phase containing significant amounts of Na, and of a median fringe (the MCL) of ankerite and (Cu,Fe) sulfide. The TML is present over the entire surface, and contains either ankerite dispersed in the clay matrix, or Cl-containing akaganeite indicating (sub)oxic conditions during the initial period of time. Akaganeite preferential formation over Cl-free phases may result from the moderate concentration of Cl^- (about 0.035 mol/kg) in the synthetic porewater (Table 1). This initial stage coincides with a significant increase in steel damage (8.5 ± 3 µm).

The three structural units (DPL, MCL, and TML) persist throughout the corrosion period, yet after 15 months, the extent and nature of DPL and TML are modified. For the DPL, magnetite is detected only at a few areas at the C-steel interface, in relative amounts decreasing with reaction time. Nanoscale characterisations have shown that a nanometric layer of a few tens of nm present at the interface can still be present and act as a barrier layer controlling the corrosion of C-steel [24-26]. Chukanovite, a Fe hydroxycarbonate, is present as well, but only after 15 months of reaction. This late formation compares with chukanovite absence for reaction times ≤ 8 months for ferrite corroding under free (non-polarized) conditions [18, 19]. In contrast, chukanovite was detected after extensive corrosion, either for archeological samples [10], for corrosion enhanced by anodic polarization [19], or for two years of free corrosion [22]. This observation hints at the possible role of chukanovite as a medium term, possibly long-term corrosion phase in nuclear waste repository. However, it also appears that chukanovite did not form a distinct structural unit, but rather was dispersed in the Fe silicate phase. At the temperature of the

312 experiment, it is unlikely that chukanovite formation could be explained by kinetics constraints alone.
313 Clearly, this phase is (meta)stable over long periods.

314 The TML evolution is marked by the disappearance of akaganeite and other Cl-rich phases after 7
315 months of reaction. Akaganeite clearly is a transient phase, and its destabilization probably corresponds to
316 slightly varying chemical conditions from the initial (sub)oxic phase (from 0 to 7 months), to reductive,
317 fully saturated conditions (>7 months). The initial suboxic conditions can explain the heterogeneity in
318 C-steel damage, as heterogeneities in oxygen concentrations could lead to galvanic decoupling [45, 46].

319 At this point, it seems that the transformation of the clay matrix in contact with C-steel is essentially
320 limited to precipitation of ankerite in clay porosity. Little to no formation of Fe-rich clay minerals has been
321 observed, contrary to mixed iron-clay slurries reacted under anoxic conditions [51-59]. The near-absence
322 of clay transformation was also observed in previous experiments using massive iron samples in bentonite
323 at 80 °C [60]. In fact, the formation of Fe silicate in clay-iron powder mixtures may relate to the high
324 surface area of powdered iron, with corrosion resulting in an important supply in dissolved Fe and OH^-.
325 The increase in pH then promotes the dissolution of silicate species and stabilizes carbonate solids, thereby
326 increasing the silicate/carbonate ratio in solution and favoring precipitation of Fe silicate. In the compact
327 massive system investigated here, precipitation of Fe silicate occurs too, but in the DPL. This leads to a
328 decrease in the pH gradient within the DPL, so that precipitation of Fe silicate in the TML is unfavourable,
329 at least over the timescale of the experiment.

330 Taken together, these results suggest that the corrosion mechanism operating at the microscopic scale
331 is gradually modified from 0 to 15 months, and then does not change significantly from 15 to 76 months.
332 This general observation is consistent with interpolations of gravimetric results. Indeed, gravimetric
333 measures fit well with an almost parabolic law for the first 15 months, consistent with a diffusion-
334 controlled corrosion regime. The diffusion-controlling medium must still be identified, and could be clay
335 or the DPL. However, this stage of CR controlled by diffusion appears to be short term. Data for the long
336 term exposure fit better with a linear law, which is consistent with a CR driven by a steady-state reaction.
337 This suggests that diffusion within clay and / or DPL has reached a steady state, which seems at odd with
338 the increasing thickness of DPL due to ongoing corrosion. A somewhat distinct behaviour was observed

for pure ferrite (Armco iron) in compact clay, i.e. a continuous decrease in CR (down to < 1 µm/year after 2 years; [22]). This discrepancy may be related to the significant impact of the metal microstructure and composition [29]. Unlike Armco iron, A-57 steel contains pearlite grains made by stacking of cementite and ferrite *lamellae*. Oxidation of the ferrite leaves cementite *lamellae*, which can act as cathodic sites, thus enhancing the cathodic reaction compared to pure ferrite [27, 28, 61]. Because these *lamellae* remain at the same positions in the DPL, the diffusion distance toward cementite does not change, explaining steady-state. Note however that there is no mineralogical evidence for the location of cathodic reaction on cementite. Another surface reaction possibly controlling the CR is the formation of a thin protective layer at the steel-CP interface [23]. This layer would form by solid-state oxidation of steel, and dissolve to form other CP at the DPL contact. Indeed magnetite is still found at the interface with steel even after 76 months exposure, possibly revealing the presence of a thinner (a few nm thick) barrier layer.

4.2 On the presence of sulfur compounds

Sulfur-containing solids were detected essentially as sulphate and Fe sulfide in the DPL, as (Fe,Cu) sulfide in the MCL, or as chalcopyrite in clay. The supply of sulphate can easily be traced to porewater. Sulfide may form by reduction of porewater sulphate, possibly by CP [62], which would result in the accumulation of this element in the DPL. Sulfide can also be supplied by pyrite reduction by H_2 released by corrosion [63], according to

$$FeS_2 + H_2 \rightarrow FeS + H_2S$$

This reaction would result in the formation of FeS and the release of sulfide. To assess the possibility of this reduction reaction, pyrite grains near the corrosion interface were examined for alteration and dissolution features. Most grains appeared to be intact, but severely altered pyrite was observed at least in one location within 100 µm of the TOSS (Figure 11). Interestingly, though, pyrite appeared to be dissolved, not replaced by Fe sulfide, suggesting a full dissolution, i.e.

$$FeS_2 + H_2 \rightarrow Fe^{2+} + 2HS^-$$

Finally, sulfide can also be supplied by sulphate reduction via the activity of sulphate-reducing prokaryotes (SRP). Indeed, the smell of hydrogen sulfide for the first series of samples suggested some

365 limited bioactivity, possibly occurring in the initial space between C-steel surfaces and holes walls. With
366 reaction time, clay swelling, and PC precipitation, however, this space collapse precluded any further
367 significant bioactivity. In fact, the location of the sulfide phase in the DPL compares with recent results on
368 the sulfidation of corrosion layers in the presence of bacteria [64]. The preferential location of Fe sulfide
369 phases in the DPL may be related to a greatest $Fe^{(II)}$ concentration in this unit coupled with a greater pH.
370 Another possibility is that sulfide preferentially precipitates within the DPL due to the interaction with
371 $Fe^{(III)}$-containing phases. Indeed, sulfide immobilization can occur via reaction with $Fe^{(III)}$-containing
372 (hydr)oxides, a reaction which takes places within weeks [65-68]. Such a reaction would be possible with
373 any residual magnetite present in the DPL.

374 Another interesting observation is the presence of Cu sulfide phase in the MCL. Copper is a trace
375 element in COX clay, with a content of 6 to 19 mg/kg, and has been observed in bulk clay as chalcopyrite.
376 Whether this Cu can be readily available for diffusion toward the C-steel surface is not clear. It can be
377 surmised however that Cu predominantly binds to organic matter [69, 70] and clay minerals [71], as in
378 soils, and so it should be fairly labile.

379 Next, Cu sulfide is much more stable than Fe sulfide such as FeS. This is illustrated by comparing the
380 dissolution reactions and constants [72] for FeS

$$FeS + 2\,H^+ = Fe^{2+} + H_2S \qquad K_{FeS} = 10^3 \qquad (3)$$

381 and CuS

$$CuS + 2\,H^+ = Cu^{2+} + H_2S \qquad K_{CuS} = 10^{-15} \qquad (4)$$

382 The much smaller K_{CuS} clearly demonstrates that this phase is very stable. Combining (3) and (4) shows
383 that FeS and CuS are at equilibrium for a concentration ratio of

$$[Fe^{2+}]/[Cu^{2+}] = K_{FeS} / K_{CuS} = 10^{18} \qquad (5)$$

384 where $[Fe^{2+}]$ and $[Cu^{2+}]$ are dissolved concentrations of Fe^{2+} and Cu^{2+}, respectively. In other words, the
385 formation of CuS is extremely favored with respect to FeS, even at trace amounts of Cu [73]. Yet, it is

surprising that Cu solid would precipitate only near the TOSS, and not in the clay. Therefore, a mechanism responsible for the preconcentration of Cu near the steel surface has to be invoked. One possible such mechanism is the reduction of Cu at cathodic sites under reducing anoxic conditions [74]. This is due to the higher electrochemical potential of the $Cu^{(II)}/Cu^{(0)}$ couple ($E^0_{Cu(II)/Cu(0)}$ = 0.33 V/SHE at 25°C) compared to the $Fe^{(II)}/Fe^{(0)}$ couple (-0.44 V/SHE at 25°C). The location of Cu reduction is then governed both by the availability of electrons, and by transport considerations dictating that Cu primarily reduces on the first encountered cathodic sites during migration. For Cu migrating from clay, these sites are located on the external parts of the C-steel sample. After DPL formation, $Cu^{(0)}$ would be insulated from steel. In principle, $Cu^{(0)}$ is stable under anoxic conditions, but it can oxidize in presence of dissolved sulfide. The oxidation mechanism would involve a first step of SH^- sorption according to [75, 76]

$$Cu^{(0)} + SH^- \Leftrightarrow Cu(SH)_{ads} + e^- , \quad (6)$$

where $Cu(SH)_{ads}$ is the chemisorbed species. The Cu surface then further reacts with SH^- leading to the formation of Cu_2S according to

$$Cu^{(0)} + Cu(SH)_{ads} + SH- \Leftrightarrow Cu_2S + H_2S + e^- , \quad (7)$$

These two anodic reactions are coupled with the cathodic reaction of proton reduction from water or H_2S. The expected formation of Cu_2S is in agreement with the chemical composition of Cu sulfide observed in the MCL (Table 5, PI 3).

The Cu sulfide fringes were also located next to the TOSS for samples with longer reacting times. No Cu is detected within the DPL, either because Cu remains located on the outer fringes, or because the concentrations are too low in this inner layer. This scarcity of Cu within the layer can have several explanations. First, this absence could simply result from an exhaustion of Cu supply from clay, so that no additional precipitate forms. Second, it may result from electron transport in the DPL to the TOSS. The nature of electron-conducing solids is not clear, but recent investigations on C-steel corroded in clay water suggest that Fe silicate can display some substantial electron-conducing properties [36].

4.3 Implications for the design of nuclear waste repository systems

Our results confirm that the limited CR observed for ferrite in contact with clay for two years also applies for C-steel in such a compact setting over six years. These rates are almost one order of magnitude lower than observed for C-steel in porewater or clay slurry [24, 77]. The discrepancy between these experiments and our compact system probably results from the much smaller diffusivity in clay, restricting the transport of reactants. Thus the CR is controlled not only by surface electrochemical reactions, but also by the diffusive transport of chemical species in the matrix and eventually by formation-dissolution of metal-CP interfacial magnetite. The net effect of this transport limitation would be to maintain a dense protective layer near the C-steel interface, limiting diffusion of Fe and oxygen. The thin layer of magnetite would be this barrier layer.

Our discussion suggests that the mechanism controlling the rate of C-steel corrosion should operate over timescales longer than our current experiments. This permits extrapolations over long periods of time of Equation 2 (LL), which can be considered conservative. After 10 and 100 years the uniform damage values of 42 µm and 320 µm (LL) are found, respectively. Calculated damage over 1000 years equal 3500 µm (LL).

5 Concluding remarks

The present study provides a unique insight into the long-term evolution of CR and the nature of CP in a compact C-steel-clay system. One salient point is the short-term coexistence of hardly corroded areas with areas of significant damage. This variability can be understood in the light of heterogeneities in clay, C-steel composition and defect distribution, and differential exposure to oxygen, leading to galvanic coupling between distinct areas. A second point of interest is the change in interfacial CP during the initial period of 13 months, meaning that corrosion processes observed prior to this time may not be relevant for long-term behavior. The implication is that investigations on the C-steel surfaces (including electrochemical ones) have to be performed on over rather long timescales to yield meaningful insight into long-term corrosion processes. Third, the CR remains constant, or even steadily decreases with increasing reaction time, and yet the proportion of C-steel surface showing significant damage increases with time. This suggests that the DPL can be somewhat protective with respect to corrosion, possibly by limiting

diffusion of dissolved species to and away from the C-steel surface and from cathodic sites. Interestingly, the CR remained near-constant although the distance between the metal-CP and the TOSS increases with time, suggesting that corrosion is not controlled by transport of reactants and products in the bulk DPL. This conclusion is in line with the presence of a nanoscale barrier of Fe oxide controlling the diffusion of atoms between C-steel and CP [23]. There is no evidence suggesting the possible onset of any new mechanism for longer reaction times.

Overall, extrapolation from damage values points to a steady to slightly decreasing rate of CR after one year. A change in corrosion regime is suggested to explain both modifications of interfaces in CP, and damage evolution within the first two years exposure, moving to a magnetite dissolution-driven regime. The rates are notably greater than those observed for pure ferrite, in agreement with some previous studies of C-steel corrosion [29]. Yet, assuming the corrosion mechanism observed after six years persists over long-term periods, a cumulated average damage of about four mm over 1000 years is calculated. This reasonable value guarantees HLW confinement over an extended time span well after the thermal peak. In principle, allowance should be made for the heterogeneous depths of corrosion depressions, for which a full mechanistic modelling is yet desirable. However, our observations suggest that generalized corrosion over the entire C-steel interface should prevail over long timescales.

6 Acknowledgements

The authors wish to acknowledge Andra, EdF, and CEA for financial support. C. Gatabin is thanked for extraction operations on the cells, D. Vantelon, J.P. Lagarde and A-M. Flank for their help during μXRD and μXAS acquisition on the LUCIA beamline, and the SOLEIL synchrotron for provision of beamtime. Finally, the authors wish to thank one anonymous reviewer for fruitful comments and corrections on the initial manuscript.

Data availability

The raw/processed data required to reproduce these findings cannot be shared at this time due to legal reasons.

References

[1] D. Féron, D. Crusset, J.M. Gras, Corrosion issue in nuclear waste disposal, J.Nucl.Mater, 379 (2008) 16-23.
[2] Andra, Évaluation de la faisabilité du stockage géologique en formation argileuse profonde. Rapport de synthèse, (2005), Andra, Chateny-Malabry (France).
[3] A. Vinsot, F. Leveau, A. Bouchet, A. Arnould, Oxidation front and oxygen transfer in the fractured zone surrounding the Meuse/Haute-Marne URL drifts in the Callovian–Oxfordian argillaceous rock, Geological Society, London, Special Publications, 400 (2014).
[4] F. King, Overview of a carbon steel container corrosion model for a deep geological repository in sedimentary rock, (2007), NWMO-TR-2007-01.
[5] S. Tricoit, Modélisation et simulation numérique de la propagation de la corrosion par piqûres du fer en milieu chloruré : contribution à l'évaluation de la durabilité des aciers au carbone en conditions de stockage géologique, Ph.D. thesis (2012), University of Dijon.
[6] D. Neff, P. Dillmann, L. Bellot-Gurlet, G. Berranger, Corrosion of iron archaeological artefacts in soil : characterisation of the corrosion system, Corros. Sci., 47 (2005) 515-535.
[7] D. Neff, P. Dillmann, M. Descostes, G. Beranger, Corrosion of iron archaeological artefacts in soil: Estimation of the average corrosion rates involving analytical techniques and thermodynamic calculations, Corros. Sci., 48 (2006) 2947-2970.
[8] D. Neff, M. Saheb, J. Monnier, S. Perrin, M. Descostes, V. L'Hostis, D. Crusset, A. Millard, P. Dillmann, A review of the archaeological analogue approaches to predict the long-term corrosion behaviour of carbon steel overpack and reinforced concrete structures in the French disposal systems, J. Nucl. Mater., 402 (2010) 196-205.
[9] D. Neff, E. Vega, P. Dillmann, M. Descostes, L. Bellot-Gurlet, G. Beranger, Contribution of iron archeological artefacts to the estimation of average corrosion rates and the long-term corrosion mechanisms of low-carbon steel buried in soils, in: P. Dillmann, G. Beranger, P. Piccardo, H. Matthiesen (Eds.) Corrosion of metallic heritage artefacts, Woodhead, Cambridge, UK, 2007, pp. 41-76.
[10] M. Saheb, D. Neff, P. Dillmann, H. Matthiesen, E. Foy, Long-term corrosion behaviour of low-carbon steel in anoxic environment: characterization of archaeological artefacts, J. Nucl. Mater., 379 (2008) 118-123.
[11] M. Saheb, M. Descostes, D. Neff, H. Matthiesen, A. Michelin, P. Dillmann, Iron corrosion in an anoxic soil: Comparison between thermodynamic modelling and ferrous archaeological artefacts characterised along with the local in situ geochemical conditions, Appl. Geochem., 25 (2010) 1937-1948.
[12] M. Saheb, D. Neff, L. Bellot-Gurlet, P. Dillmann, Raman study of a deuterated iron hydroxycarbonate to assess long-term corrosion mechanisms in anoxic soils, J. Raman Spectrosc., 42 (2011) 1100-1108.
[13] F.T. Madsen, Clay mineralogical investigations related to nuclear waste disposal, Clay Min., 33 (1998) 109-129.
[14] L. Carlson, O. Karnland, V.M. Oversby, A.P. Rance, N.R. Smart, M. Snellman, M. Vahanen, L.O. Werme, Experimental studies of the interactions between anaerobically corroding iron and bentonite, Phys. Chem. Earth, 32 (2007) 334-345.
[15] N.R. Smart, A.P. Rance, L.O. Werme, The effect of radiation on the anaerobic corrosion of steel, J. Nucl. Mater., 379 (2008) 97-104.
[16] C. Bataillon, C. Musy, M. Roy, Corrosion des surconteneurs de déchets, cas d'un surconteneur en acier faiblement allié., J. Phys. IV, 11 (2001) 267-274.
[17] F.A. Martin, C. Bataillon, M.L. Schlegel, Corrosion of iron and low alloyed steel within a water saturated brick of clay under anaerobic deep geological disposal conditions: An integrated experiment, J. Nucl. Mater., 379 (2008) 80-90.
[18] M.L. Schlegel, C. Bataillon, K. Benhamida, C. Blanc, D. Menut, J.-L. Lacour, Metal corrosion and argillite transformation at the water-saturated, high temperature iron-clay interface: a microscopic-scale study, Appl. Geochem., 23 (2008) 2619-2633.
[19] M.L. Schlegel, C. Bataillon, C. Blanc, D. Prêt, E. Foy, Anodic activation of iron corrosion in clay media under water-saturated conditions at 90 °C: characterization of the corrosion interface, Environ. Sci. Technol., 44 (2010) 1503-1508.
[20] G. de Combarieu, P. Barboux, Y. Minet, Iron corrosion in Callovo-Oxfordian argilite: From experiments to thermodynamic/kinetic modelling, Phys. Chem. Earth, 32 (2007) 346-358.

[21] G. de Combarieu, M.L. Schlegel, D. Neff, E. Foy, D. Vantelon, P. Barboux, S. Gin, Glass-Iron-Clay interaction in a radioactive waste geological disposal: an integrated laboratory-scale experiment, Appl. Geochem., 26 (2011) 65-79.
[22] M.L. Schlegel, C. Bataillon, F. Brucker, C. Blanc, D. Prêt, E. Foy, M. Chorro, Corrosion of metal iron in contact with anoxic clay at 90 °C: characterization of the corrosion products after two years of interaction, Appl. Geochem., 51 (2014) 1-14.
[23] C. Bataillon, F. Bouchon, C. Chainais-Hillairet, C. Desgranges, E. Hoarau, F. Martin, S. Perrin, M. Tupin, J. Talandier, Corrosion modelling of iron based alloy in nuclear waste repository, Electrochim. Acta, 55 (2010) 4451-4467.
[24] Y. Leon, P. Dillmann, D. Neff, M.L. Schlegel, E. Foy, J.J. Dynes, Interfacial layers at a nanometre scale on iron corroded in carbonated anoxic environments, RSC Adv., 7 (2017) 20101-20115.
[25] Y. Leon, M. Saheb, E. Drouet, D. Neff, E. Foy, E. Leroy, J.J. Dynes, P. Dillmann, Interfacial layer on archaeological mild steel corroded in carbonated anoxic environments studied with coupled micro and nano probes, Corros. Sci., 88 (2014) 23-35.
[26] A. Michelin, E. Drouet, E. Foy, J.J. Dynes, D. Neff, P. Dillmann, Investigation at the nanometre scale on the corrosion mechanisms of archaeological ferrous artefacts by STXM, J. Anal. At. Spectrom., 28 (2013) 59-66.
[27] J.-L. Crolet, N. Thevenot, S. Nesic, Role of conductive corrosion products in the protectiveness of corrosion layers, Corrosion, 54 (1998) 194-202.
[28] D.N. Staicopolus, The role of cementite in the acidic corrosion of steel, J. Electrochem. Soc., 110 (1963) 1121-1124.
[29] S. Al-Hassan, B. Mishra, D.L. Olson, M.M. Salama, Effect of microstructure on corrosion of steels in aqueous solutions containing carbon dioxide, Corrosion, 54 (1998) 480-491.
[30] F. Martin, S. Perrin, M. Fenart, M. Schlegel, C. Bataillon, On corrosion of carbon steels in Callovo-Oxfordian clay: complementary EIS, gravimetric and structural study providing insights on long term behaviour in French geological disposal conditions, Corr. Eng. Sci. Technol., 49 (2014) 460-466.
[31] E. Gaucher, C. Robelin, J.M. Matray, G. Negral, Y. Gros, J.F. Heitz, A. Vinsot, H. Rebours, A. Cassagnabere, A. Bouchet, ANDRA underground research laboratory: interpretation of the mineralogical and geochemical data acquired in the Callovian-Oxfordian formation by investigative drilling, Phys. Chem. Earth, 29 (2004) 55-77.
[32] M. Descostes, V. Blin, F. Bazer-Bachi, P. Meier, B. Grenut, J. Radwan, M.L. Schlegel, S. Buschaert, D. Coelho, E. Tevissen, Diffusion of anionic species in Callovo-Oxfordian argillites and Oxfordian limestones (Meuse-Haute Marne, France), Appl. Geochem., 23 (2008) 655-677.
[33] E.C. Gaucher, P. Blanc, F. Bardot, G. Braibant, S. Buschaert, C. Crouzet, A. Gautier, J.P. Girard, E. Jacquot, A. Lassin, G. Negrel, C. Tournassat, A. Vinsot, S. Altmann, Modelling the porewater chemistry of the Callovian-Oxfordian formation at a regional scale, Comptes Rendus Geoscience, 338 (2006) 917-930.
[34] A. Vinsot, J. Delay, In situ sampling and characterization of Callovo-Oxfordian pore water,12th International Symposium on Water-Rock Interaction (WRI-12), Kunming, P.R. China, 2007, in: T.D. Bullen, Y. Wang (Eds.), Taylor & Francis, London, 663-666.
[35] M.L. Schlegel, S. Necib, S. Daumas, C. Blanc, E. Foy, N. Trcera, A. Romaine, Microstructural characterization of carbon steel corrosion in clay borehole water,under anoxic and transient acidic conditions, Corros. Sci., 109 (2016) 126-144.
[36] M.L. Schlegel, S. Necib, S. Daumas, M. Labat, C. Blanc, E. Foy, Y. Linard, Corrosion at the carbon steel-clay borehole water and gas interfaces at 85 °C under anoxic alkaline conditions, Corros. Sci., 136 (2018) 70-90.
[37] A.P. Hammersley, FIT2D: a multi-purpose data reduction, analysis and visualization program, J. Appl. Cryst., 49 (2016) 646-652.
[38] A.M. Flank, G. Cauchon, P. Lagarde, S. Bac, M. Janousch, R. Wetter, J.M. Dubuisson, M. Idir, F. Langlois, T. Moreno, D. Vantelon, LUCIA, a microfocus soft XAS beamline, Nucl. Instrum. Methods Phys. Res. B, 246 (2006) 269-274.
[39] L. Tröger, E. Zschech, D. Arvanitis, K. Baberschke, Quantitative fluorescence EXAFS analysis of concentrated samples-correction of the self-absorption effect,7th International Conference on X-Ray Absorption Fine Structure, Kobe, Japan, 1992, in, 144-146.

[40] L. Tröger, D. Arvanitis, K. Baberschke, H. Michaelis, U. Grimm, E. Zschech, Full correction of the self-absorption effect in soft-fluorescence exended x-ray-absorption fine structure, Phys. Rev. B, 46 (1992) 3283-3289.
[41] B.K. Teo, EXAFS: basic principles and data analysis, Springer-Verlag, Berlin, Germany, 1986.
[42] B. Ravel, M. Newville, ATHENA, ARTEMIS, HEPHAESTUS: data analysis for X-ray absorption spectroscopy using IFEFFIT, J. Synchrotron Rad., 12 (2005) 537-541.
[43] M. Newville, IFEFFIT: interactive XAFS analysis and FEFF fitting, J. Synchrotron Rad., 8 (2001) 322-324.
[44] M. Newville, EXAFS analysis using FEFF and FEFFIT, J. Synchrotron Rad., 8 (2001) 96-100.
[45] B.W.A. Sherar, P.G. Keech, D.W. Shoesmith, Carbon steel corrosion under anaerobic-aerobic cycling conditions in near-neutral pH saline solutions - Part 1: Long term corrosion behaviour, Corros. Sci., 53 (2011) 3636-3642.
[46] B.W.A. Sherar, P.G. Keech, D.W. Shoesmith, Carbon steel corrosion under anaerobic-aerobic cycling conditions in near-neutral pH saline solutions. Part 2: Corrosion mechanism, Corros. Sci., 53 (2011) 3643-3650.
[47] D. Li, G.M. Bancroft, M.E. Fleet, X.H. Feng, Silicon K-Edge XANES spectra of silicate minerals, Phys. Chem. Minerals, 22 (1995) 115-122.
[48] M.E. Fleet, XANES spectroscopy of sulfur in earth materials, Can. Miner., 43 (2005) 1811-1838.
[49] J. Prietzel, A. Botzaki, N. Tyufekchieva, M. Brettholle, J. Thieme, W. Klysubun, Sulfur speciation in soil by S K-Edge XANES spectroscopy: comparison of spectral deconvolution and linear combination fitting, Environ. Sci. Technol., 45 (2011) 2878-2886.
[50] J.L. Alamilla, M.A. Espinosa-Medina, E. Sosa, Modelling steel corrosion damage in soil environment, Corros. Sci., 51 (2009) 2628-2638.
[51] R. Mosser-Ruck, I. Pignatelli, F. Bourdelle, M. Abdelmoula, O. Barres, D. Guillaume, D. Charpentier, D. Rousset, M. Cathelineau, N. Michau, Contribution of long-term hydrothermal experiments for understanding the smectite-to-chlorite conversion in geological environments, Contrib. Mineral. Petrol., 171 (2016) art.97.
[52] I. Pignatelli, F. Bourdelle, D. Bartier, R. Mosser-Ruck, L. Truche, E. Mugnaioli, N. Michau, Iron-clay interactions: Detailed study of the mineralogical transformation of claystone with emphasis on the formation of iron-rich T-O phyllosilicates in a step-by-step cooling experiment from 90 °C to 40 °C, Chem. Geol., 387 (2014) 1-11.
[53] I. Pignatelli, E. Mugnaioli, J. Hybler, R. Mosser-Ruck, M. Cathelineau, N. Michau, A multi-step technique characterization of cronstedtite synthesized by iron-clay interaction in a step-by-step cooling procedure, Clays Clay Min., 61 (2013) 277-289.
[54] D. Charpentier, K. Devineau, R. Mosser-Ruck, M. Cathelineau, F. Villieras, Bentonite-iron interactions under alkaline condition: An experimental approach, Appl. Clay Sci., 32 (2006) 1-13.
[55] F. Bourdelle, R. Mosser-Ruck, L. Truche, C. Lorgeoux, I. Pignatelli, N. Michau, A new view on iron-claystone interactions under hydrothermal conditions (90°C) by monitoring in situ pH evolution and H_2 generation, Chem. Geol., 466 (2017) 600-607.
[56] P. Le Pape, C. Rivard, M. Pelletier, I. Bihannic, R. Gley, S. Mathieu, L. Salsi, S. Migot, O. Barres, F. Villieras, N. Michau, Action of a clay suspension on an Fe(0) surface under anoxic conditions: Characterization of neoformed minerals at the Fe(0)/solution and Fe(0)/atmosphere interfaces, Appl. Geochem., 61 (2015) 62-71.
[57] C. Rivard, E. Montarges-Pelletier, D. Vantelon, M. Pelletier, C. Karunakaran, L.J. Michot, F. Villieras, N. Michau, Combination of multi-scale and multi-edge X-ray spectroscopy for investigating the products obtained from the interaction between kaolinite and metallic iron in anoxic conditions at 90 °C, Phys. Chem. Minerals, 40 (2013) 115-132.
[58] C. Rivard, M. Pelletier, N. Michau, A. Razafitianamaharavo, M. Abdelmoula, J. Ghanbaja, F. Villiéras, Reactivity of Callovo-Oxfordian claystone and its clay fraction with metallic iron: role of non-clay minerals in the interaction mechanism, Clays Clay Min., 63 (2015) 290-310.
[59] B. Lanson, S. Lantenois, P.A. van Aken, A. Bauer, A. Plancon, Experimental investigation of smectite interaction with metal iron at 80°C: Structural characterization of newly formed Fe-rich phyllosilicates, Am. Miner., 97 (2012) 864-871.

[60] T. Ishidera, K. Ueno, S. Kurosawa, T. Suyama, Investigation of montmorillonite alteration and form of iron corrosion products in compacted bentonite in contact with carbon steel for ten years, Phys. Chem. Earth, 33 (2008) S269-S275.
[61] X.H. Hao, J.H. Dong, I.I.N. Etim, J. Wei, W. Ke, Sustained effect of remaining cementite on the corrosion behavior of ferrite-pearlite steel under the simulated bottom plate environment of cargo oil tank, Corros. Sci., 110 (2016) 296-304.
[62] C. Mansour, G. Berger, M. Fédoroff, G. Lefèvre, Pages, A., E.M. Pavageau, H. Catalette, S. Zanna, Influence of temperature and reducing conditions on the sorption of sulfate on magnetite, J. Colloid Interf. Sci., 352 (2010) 476-482.
[63] L. Truche, G. Berger, C. Destrigneville, D. Guillaume, E. Giffaut, Kinetics of pyrite to pyrrhotite reduction by hydrogen in calcite buffered solutions between 90 and 180°C: Implications for nuclear waste disposal, Geochim. Cosmochim. Acta, 74 (2010) 2894-2914.
[64] M. Etique, A. Romaine, I. Bihannic, R. Gley, C. Carteret, M. Abdelmoula, C. Ruby, M. Jeannin, R. Sabot, P. Refait, F.P.A. Jorand, Abiotically or microbially mediated transformations of magnetite by sulphide species: The unforeseen role of nitrate-reducing bacteria, Corros. Sci., 142 (2018) 31-44.
[65] D.E. Canfield, R. Raiswell, S. Bottrell, The reactivity of sedimentary iron minerals toward sulfide, Am. J. Sci., 292 (1992) 659-683.
[66] M. Dos Santos Afonso, W. Stumm, Reductive dissolution of iron(III) (hydr)oxides by hydrogen sulfide, Langmuir, 8 (1992) 1671-1675.
[67] S.W. Poulton, M.D. Krom, R. Raiswell, A revised scheme for the reactivity of iron (oxyhydr)oxide minerals towards dissolved sulfide, Geochim. Cosmochim. Acta, 68 (2004) 3703-3715.
[68] D.E. Canfield, R.A. Berner, Dissolution and pyritization of magnetite in anoxic marine sediments, Geochim. Cosmochim. Acta, 51 (1987) 645-659.
[69] A.R. Jacobson, S. Dousset, F. Andreux, P.C. Baveye, Electron microprobe and synchrotron X-ray fluorescence mapping of the heterogeneous distribution of copper in high-copper vineyard soils, Environ. Sci. Technol., 41 (2007) 6343-6349.
[70] D.G. Strawn, L.L. Baker, Speciation of Cu in a contaminated agricultural soil measured by XAFS, μ-XAFS, and μ-XRF, Environ. Sci. Technol., 42 (2008) 37-42.
[71] M.F. Hochella, J.N. Moore, C.V. Putnis, A. Putnis, T. Kasama, D.D. Eberl, Direct observation of heavy metal-mineral association from the Clark Fork River Superfund Complex: Implications for metal transport and bioavailability, Geochim. Cosmochim. Acta, 69 (2005) 1651-1663.
[72] J.D. Allison, D.S. Brown, K.J. Novo-Gradac, MINTEQA2/PRODEFA2- A geochemical assesment model for environmental systems, (1990), Athens, Georgia.
[73] F.A. Weber, A. Voegelin, R. Kretzschmar, Multi-metal contaminant dynamics in temporarily flooded soil under sulfate limitation, Geochim. Cosmochim. Acta, 73 (2009) 5513-5527.
[74] M. Saheb, D. Neff, C. Bataillon, E. Foy, P. Dillmann, Copper tracing to determine the micrometric electronic properties of a thick ferrous corrosion layer formed in an anoxic medium, Corros. Sci., 53 (2011) 2201-2207.
[75] J. Chen, Z. Qin, D.W. Shoesmith, Kinetics of corrosion film growth on copper in neutral chloride solutions containing small concentrations of sulfide, J. Electrochem. Soc., 157 (2010) C338-C345.
[76] J. Chen, Z. Qin, D.W. Shoesmith, Long-term corrosion of copper in a dilute anaerobic sulfide solution, Electrochim. Acta, 56 (2011) 7854-7861.
[77] S. Necib, Y. Linard, D. Crusset, N. Michau, S. Daumas, E. Burger, A. Romaine, M.L. Schlegel, Corrosion at the carbon steel-clay borehole water and gas interfaces at 85°C under anoxic and transient acidic conditions, Corros. Sci., 111 (2016) 242-258.

7 Figure captions

Figure 1. (a) Schematic illustration of the three types of sample geometry used in the Corridda setup. (b) Schematic illustration and (c) image of the geometry containment for three massive probes in a clay cylinder (upper argillite lid removed in the image). (d) Schematic illustration of the Corridda setup.

Figure 2. Sample damage as a function of reaction time for the massive rods (■). Also illustrated are the fits of experimental data with logarithmic law, power law and linear law.

Figure 3. Scanning electron image in Backscattered Electron (BSE) mode of the steel-clay corrosion interface as a function of reaction time. DPL: dense product layer. MCL: median corrosion layer; TML: transformed matrix layer. (a-c) C06, 7 months of reaction. (d) C12, 27 months of reaction. (e) C15, 40 months of reaction. (f) C18, 76 months of reaction.

Figure 4. (a) EDX chemical map for the Cl-poor steel-clay interfaces of C06 sample (7 months of reaction). (b) µXRD diagram for the Cl-poor steel-clay interfaces for C06.

Figure 5. (a). EDX chemical map for the Cl-rich steel-clay interface of the C06 sample (7 months of reaction). (b,c) µRaman spectra at selected Raman PI for the Cl-rich steel-clay interfaces of C06.

Figure 6. Examples of EDX chemical map for the steel-clay interface for 15 to 76 months of reaction. Points of Interest analyzed by EDX spectrometry are indicated on the BSE images.

Figure 7. Optical image and µRS data for the steel-clay corrosion interface (27 months of reaction).

Figure 8. (a) BSE image of the DPL layer at the carbon-steel corrosion interface of the C15 sample (40 months of reaction), with location of the area probed by µXRF (square). (b) µXRF image of Si distribution at the steel-clay interface. The local Si concentration is in “temperature” scale (violet: lowest – red: highest). Also indicated are the PI probed by µXAFS spectroscopy. (c) Si K-edge spectra of reference compounds and at PI in the DPL layer (PI X1-X4), and in the TML (X5-X6).

Figure 9. (a) BSE image of the DPL layer at the steel-clay corrosion interface (C15 sample, 40 months of reaction). (b) SEM-EDX raw-count map of Si distribution in intensity scale (yellow-highest concentration). (c) µXRF image of S distribution at the steel-clay interface, and PI analyzed by µXAFS spectroscopy. The local S concentration is in “temperature” scale (violet: lowest – red: highest). (d) Sulfur K-edge spectra of PI in the DPL layer.

Figure 10. (a) SEM-BSE image of the carbon-steel Median Corrosion Layer (MCL) (C12 sample, 27 months of reaction), with location of the PI probed by µRS. (b,c) micro-Raman spectra at the PI of the MCL.

Figure 11. BSE image of a pyrite grain near the steel-clay interface, with clear evidence of alteration features.

8 Tables

Table 1. Composition of the synthetic porewater used in this study.

Species	Concentration (mmol/kg)
Na^+	7.3
K^+	2.5
Mg^{2+}	6.5
Ca^{2+}	8.6
$Si(OH)_4$	0.1
HCO_3^-	1.6
Cl^-	35
SO_4^{2-}	1.7

Table 2. Samples investigated in this study.

Name	Reaction time
C06	7 month
C09	13 months
C12	27 months
C15	40 months
C18	76 months

714

Table 3. Quantification of SEM-EDX analyses of CP present at the "Cl-poor" steel-clay interface of the C06 sample (7 months). The corresponding points of Interest (PI) are illustrated in Figure 4.

PI	Composition (at.%)									
	O	Na	Mg	Al	Si	S	Cl	K	Ca	Fe
1	73.5	0.8	0.1	0.1	0.9	0.6	0	0	1.3	22.6
2	76.4	1.6	0.1	0.1	8.1	0.6	0	0.1	0.5	12.6
3	77	1.4	0	0.1	7.3	0.5	0	0.1	0.5	13.1
4	78.8	0.8	0.1	0.1	3.3	0.7	0	0	3.5	12.7
5	77.2	0.8	0.1	0.2	1.2	0.6	0	0.1	2.4	17.5
6	77.3	0.2	0.5	1.6	3.2	0.2	0.1	0.4	6.2	9.7

715

716

717

Table 4. Quantification of SEM-EDX analyses of CP present at the "Cl-rich" steel-clay interface of the C06 sample (7 months). The corresponding PI are illustrated in Figure 5.

PI	Composition (at.%)									
	O	Na	Mg	Al	Si	S	Cl	K	Ca	Fe
1	75.2	1.6	0	0.1	1.4	0.3	0	0	0.9	20.5
2	73.6	1.1	0	0.1	1.3	0.3	0	0.1	0.8	22.7
3	76.2	0.6	0.4	0.6	2.7	0.2	0	0.1	5.2	14
4	78.4	0.2	0	0.1	0.2	0.5	0.7	0	0.3	19.5
5	76.2	0.2	0	0.2	0.5	0.4	0.9	0.1	0.2	21.4

718

719

Table 5. Quantification of SEM-EDX analyses of CP present at the steel-clay interface of the samples reacted from 15 to 76 months. The corresponding PI are illustrated in Figure 6.

Sample Name	PI	Composition (at.%)										
		O	Na	Mg	Al	Si	S	Cl	K	Ca	Fe	Cu
C09	1	69.9	0.1	0.1	0.9	4.9	0.7	0	0	0.3	22.7	n.m.[a]
	2	64.1	0.6	0.3	1.1	9.1	2.5	0.1	0.2	0.2	20.9	0
	3	3.8	0.	0.1	3.3	0.7	28.2	0.1	0	0.2	14.6	49.0
	4	75.1	0.3	0.6	2.0	2.0	0.2	0.2	0.2	4.6	14.9	0.2
C12	5	68.7	1.2	0.5	0.1	7.2	0.8	0	0	0.2	21.2	n.m.
	6	63.1	1.5	0.8	0.1	10.7	1.7	0.1	0.1	0.5	21.4	n.m.
	7	60.1	1.6	1.0	0	18.1	1.3	0	0.1	0.2	17.6	n.m.
	8	78.4	0.6	2.5	0	0.2	0.2	0	0	5.8	12.0	n.m.
C18	9	67.6	0.6	0.3	0.4	13.4	1.1	0.1	0	0.2	15.8	0.4
	10	56.2	0.6	0.9	1.1	20.9	1.6	0.6	0	1.2	16.4	0.4
	11	72.3	0.1	1.6	0	0.1	0.1	0	0	5.2	20.6	0.1

720 [a]: n.m.: not measured

721

722

723

Table 6. Comparison of the average corrosion damage at the steel-clay interface from systematic measurements of damage thickness and from gravimetric measurements.

Reaction time (months)	Direct measurements			Gravimetric measurements	
	Number of measurments	Damage thickness (µm)	Dispersion (µm)	Damage thickness (µm)	Standard deviation (µm)
7	325	12	9	8.5	0.8
13	360	19	12	12.7	2.6
27	360	25	18	13.5	2.4
40	360	16	13	18.2	3.7
76	360	43	21	29.5	1.0

724

725

Figures

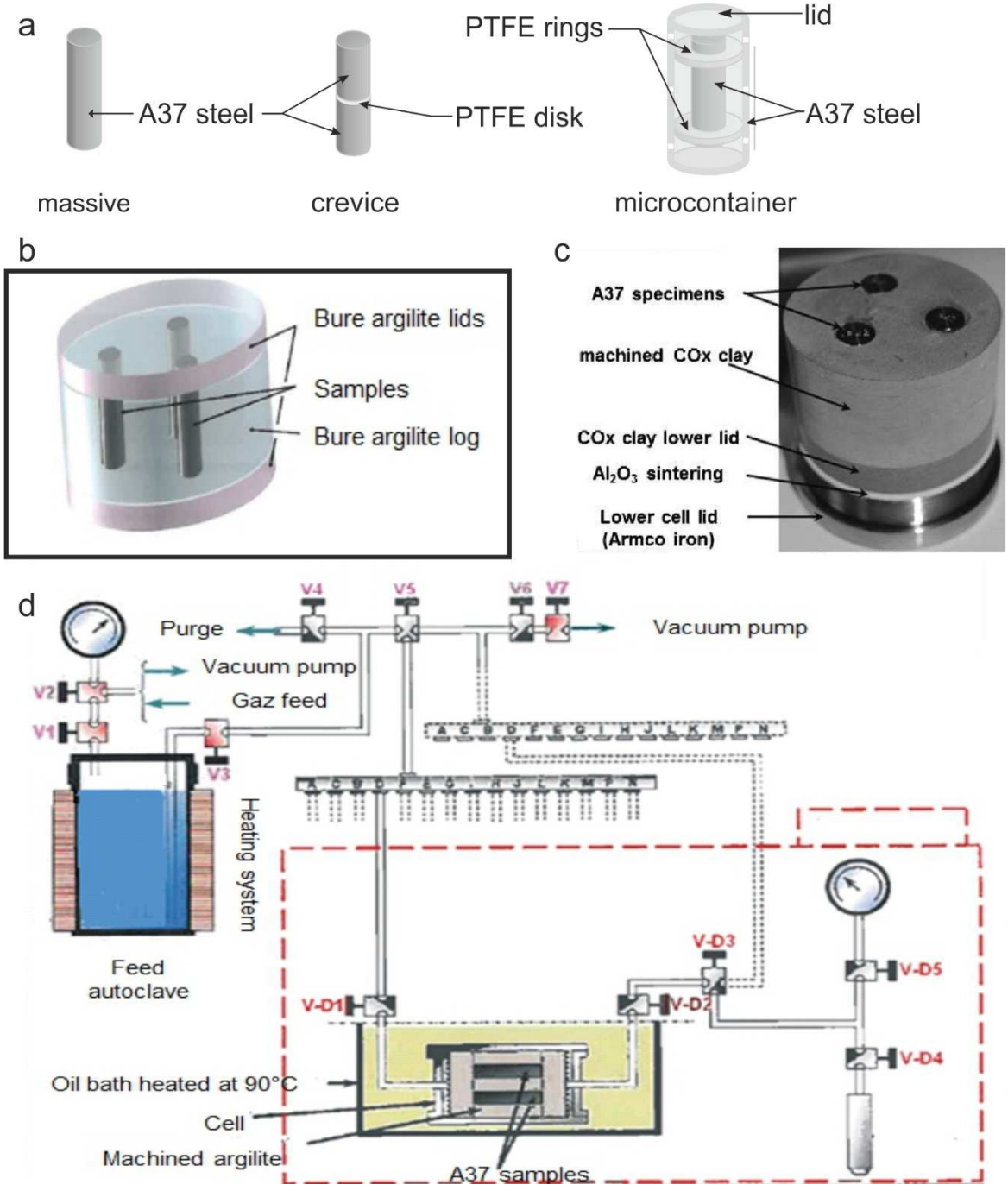

Figure 1. (a) Schematic illustration of the three types of sample geometry used in the Corridda setup. (b) Schematic illustration and (c) image of the geometry containment for three massive probes in a clay cylinder (upper argillite lid removed in the image). (d) Schematic illustration of the Corridda setup.

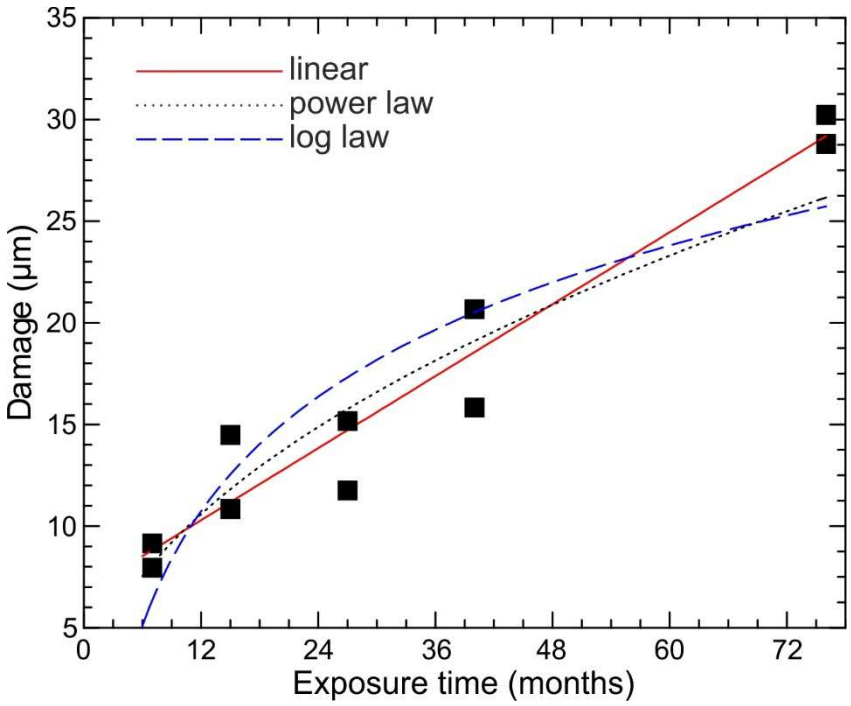

734

735

736 Figure 2. Sample damage as a function of reaction time for the massive rods (■). Also illustrated are
737 the fits of experimental data with logarithmic law, power law and linear law.

738

739

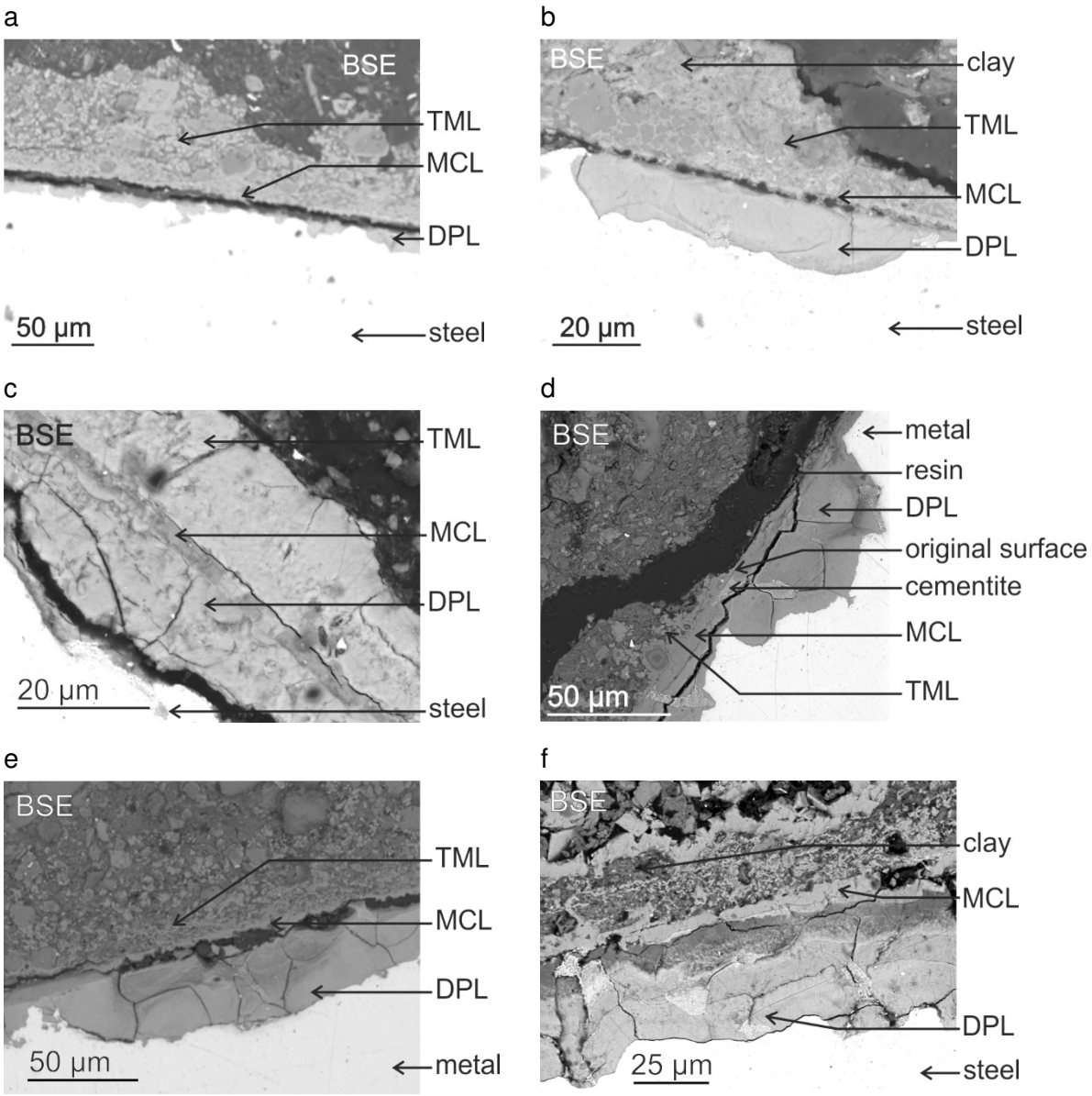

740

741 Figure 3. Scanning electron image in Backscattered Electron (BSE) mode of the steel-clay corrosion
742 interface as a function of reaction time. DPL: dense product layer. MCL: median corrosion layer;
743 TML: transformed matrix layer. (a-c) C06, 7 months of reaction. (d) C12, 27 months of reaction. (e)
744 C15, 40 months of reaction. (f) C18, 76 months of reaction.

745

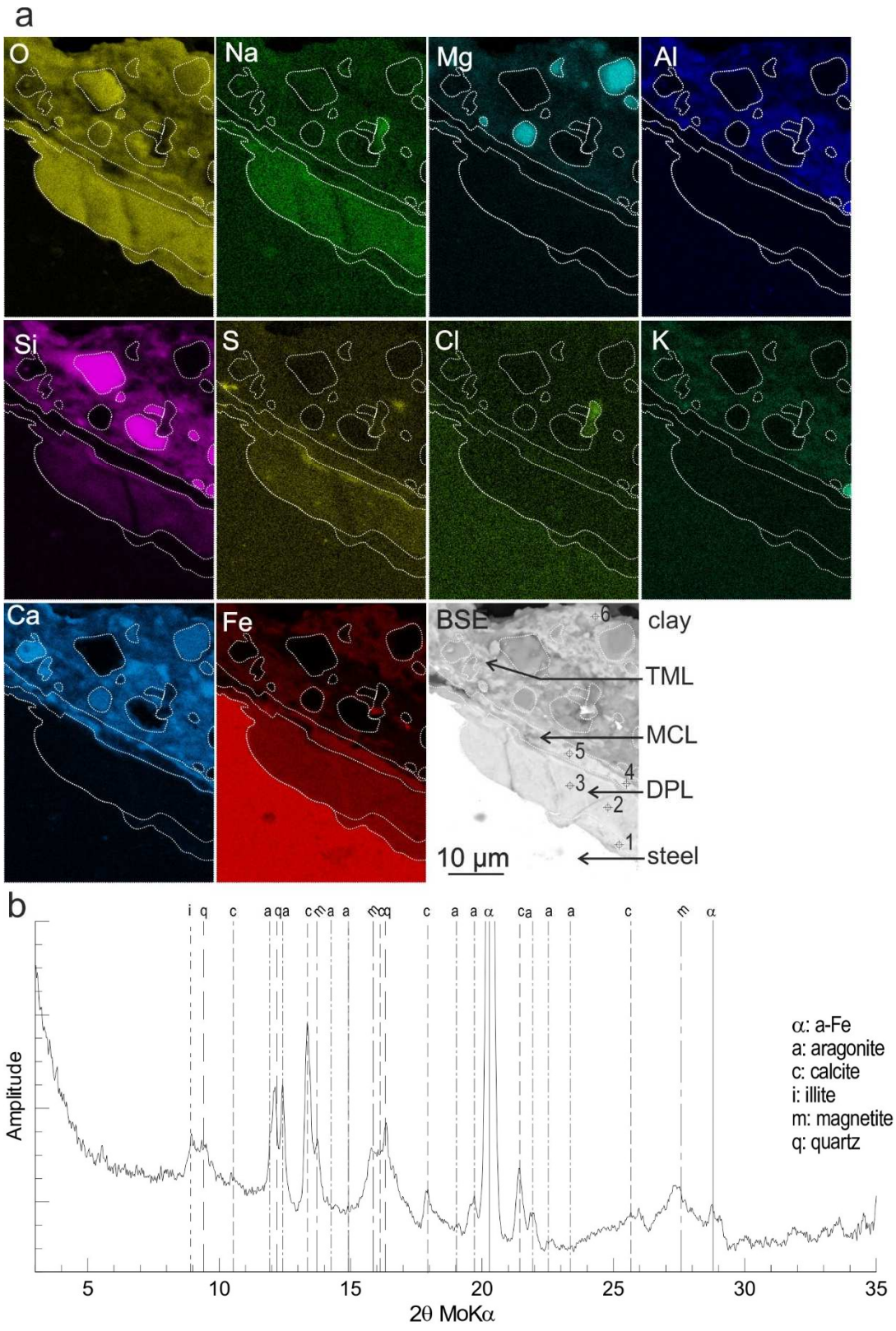

746

747 Figure 4. (a) EDX chemical map for the Cl-poor steel-clay interfaces of C06 sample (7 months of
748 reaction). (b) µXRD diagram for the Cl-poor steel-clay interfaces for C06.

749

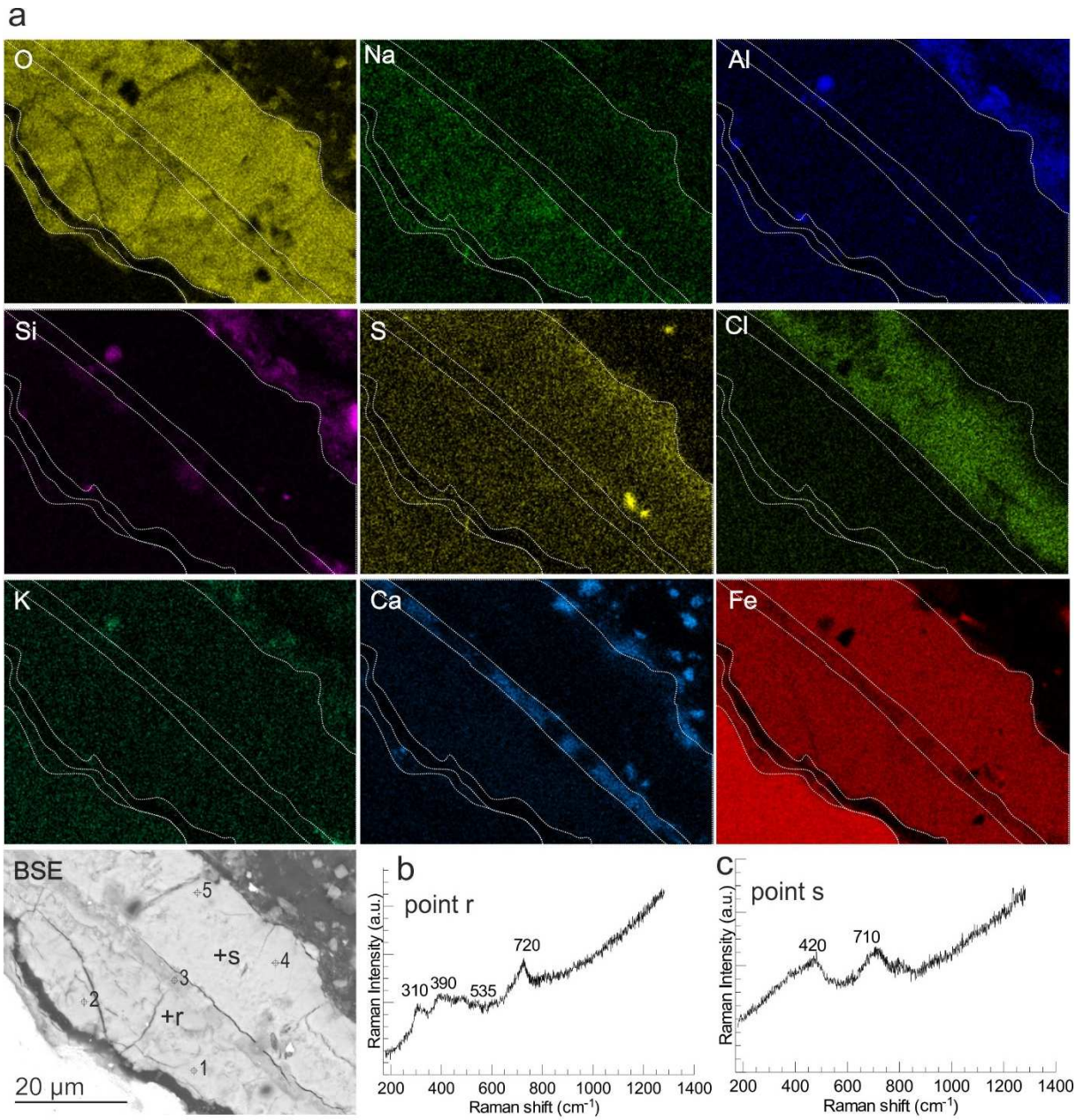

750

751 Figure 5. (a). EDX chemical map for the Cl-rich steel-clay interface of the C06 sample (7 months of
752 reaction). (b,c) µRaman spectra at selected Raman PI for the Cl-rich steel-clay interfaces of C06.

753

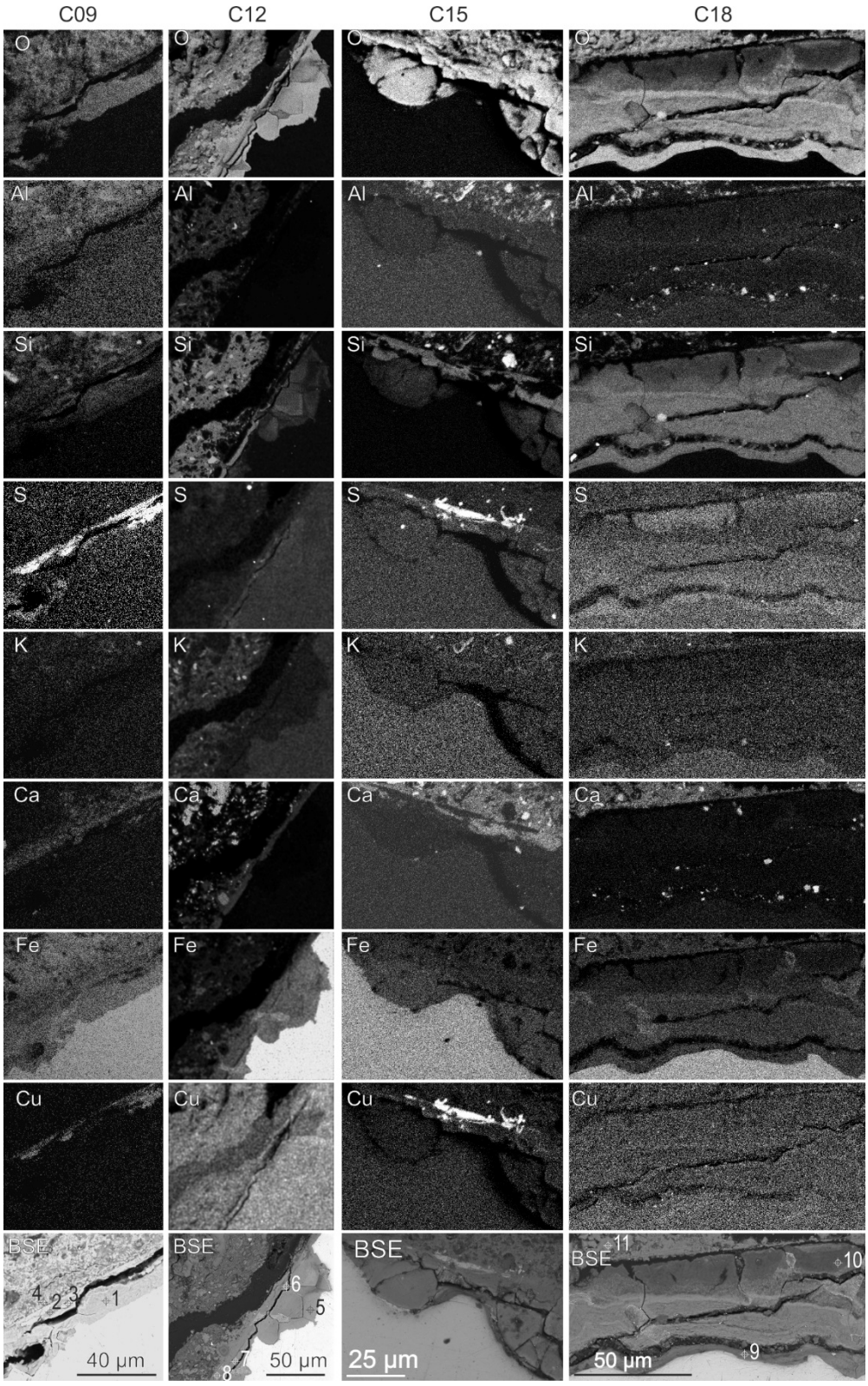

754

755 Figure 6. Examples of EDX chemical map for the steel-clay interface for 15 to 76 months of reaction.
756 Points of Interest analyzed by EDX spectrometry are indicated on the BSE images.

757

758

759

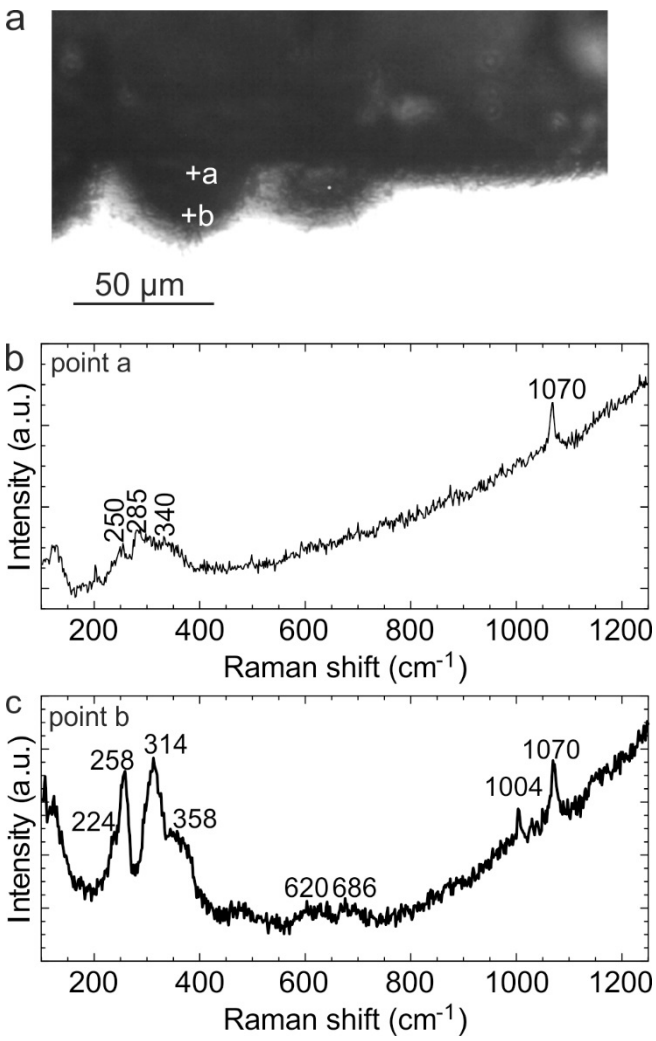

760

761 Figure 7. Optical image and µRS data for the steel-clay corrosion interface (27 months of reaction).

762

763

764

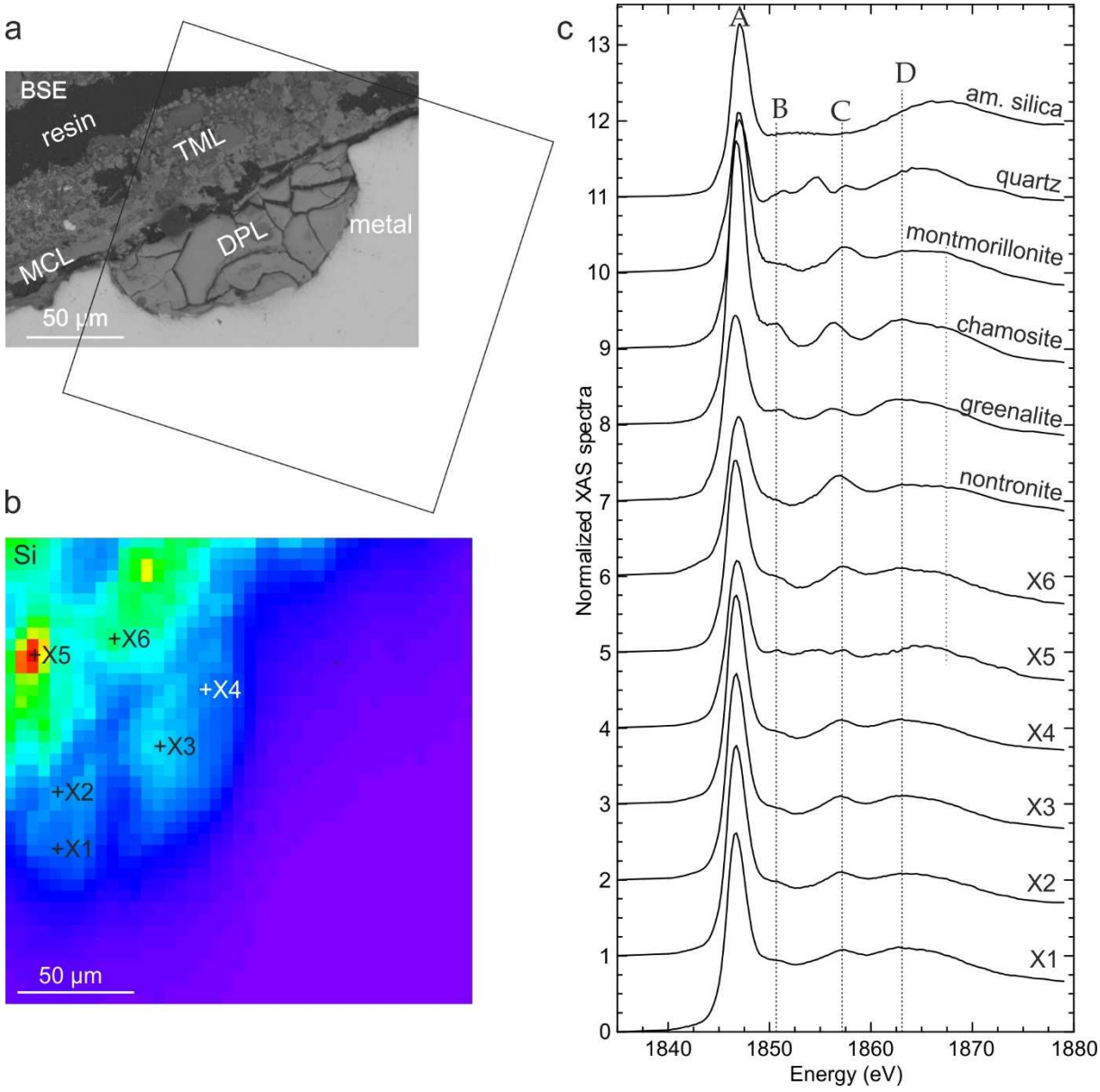

765

766 Figure 8. (a) BSE image of the DPL layer at the carbon-steel corrosion interface of the C15 sample (40
767 months of reaction), with location of the area probed by µXRF (square). (b) µXRF image of Si
768 distribution at the steel-clay interface. The local Si concentration is in "temperature" scale (violet:
769 lowest – red: highest). Also indicated are the PI probed by µXAFS spectroscopy. (c) Si K-edge spectra
770 of reference compounds and at PI in the DPL layer (PI X1-X4), and in the TML (X5-X6).

771

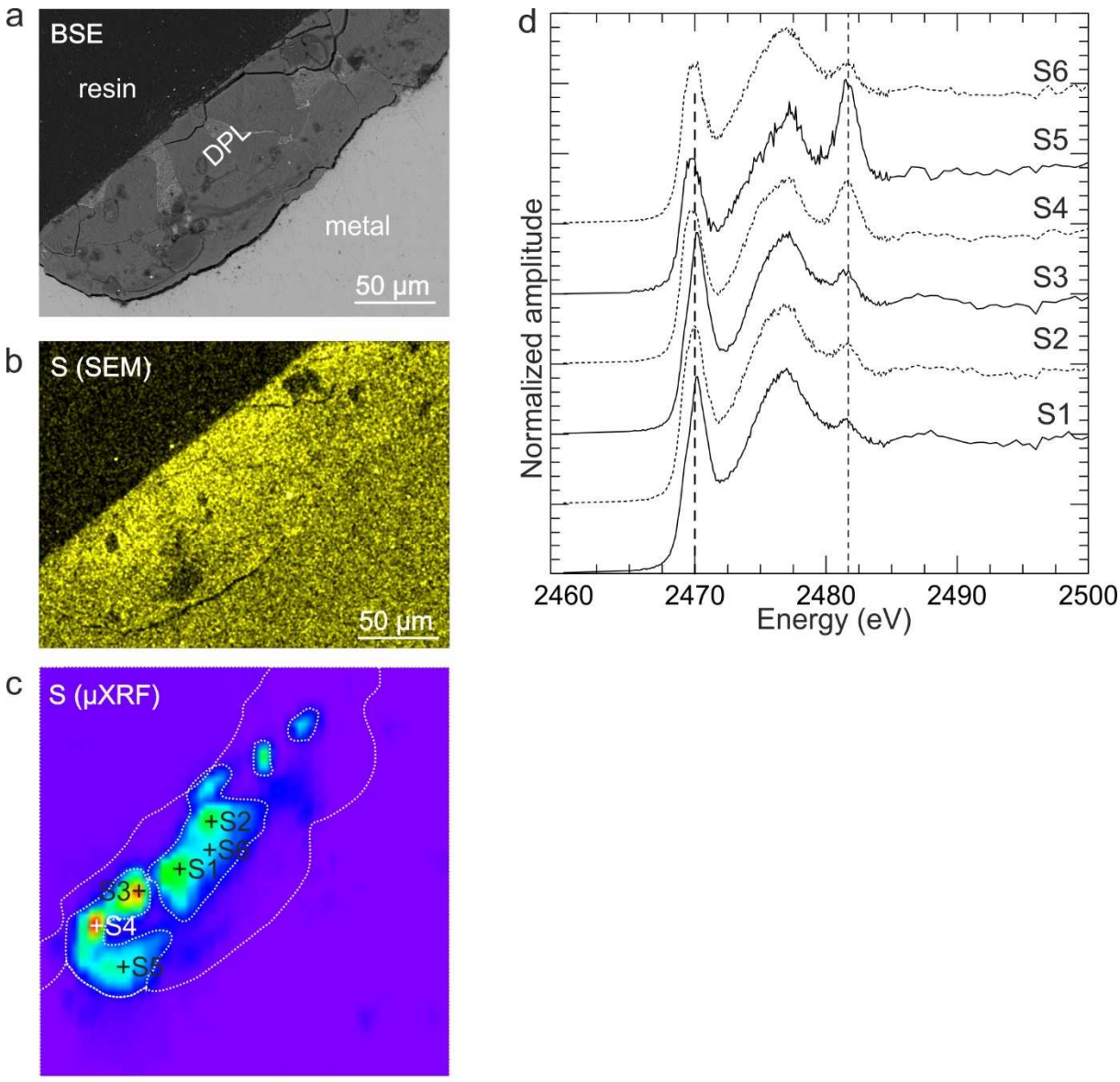

772

773

774 Figure 9. (a) BSE image of the DPL layer at the steel-clay corrosion interface (C15 sample, 40 months
775 of reaction). (b) SEM-EDX raw-count map of Si distribution in intensity scale (yellow-highest
776 concentration). (c) µXRF image of S distribution at the steel-clay interface, and PI analyzed by
777 µXAFS spectroscopy. The local S concentration is in "temperature" scale (violet: lowest – red:
778 highest). (d) Sulfur K-edge spectra of PI in the DPL layer.

779

780

781

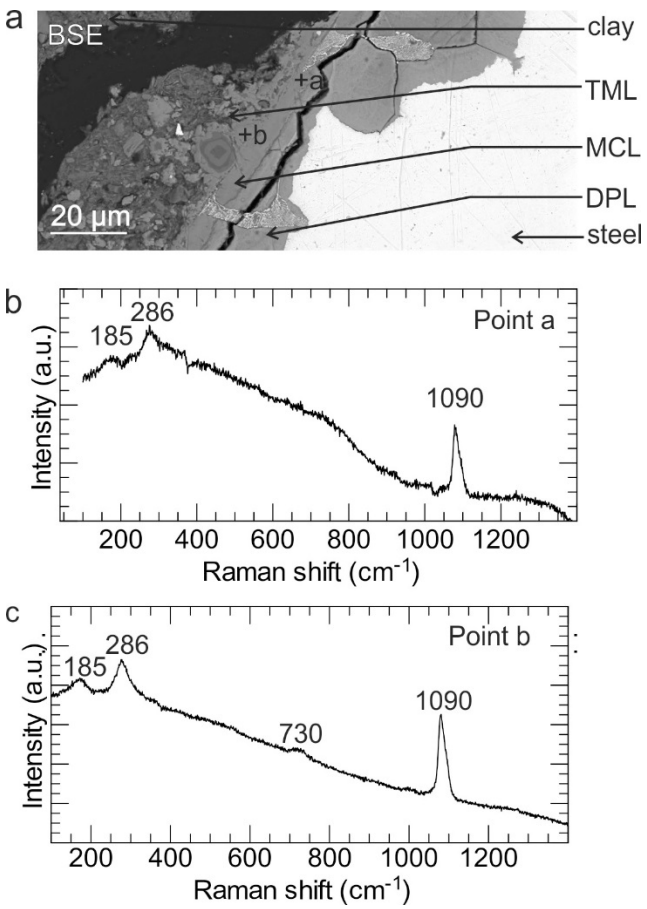

782

783 Figure 10. (a) SEM-BSE image of the carbon-steel Median Corrosion Layer (MCL) (C12 sample, 27
784 months of reaction), with location of the PI probed by µRS. (b,c) micro-Raman spectra at the PI of
785 the MCL.

786

787

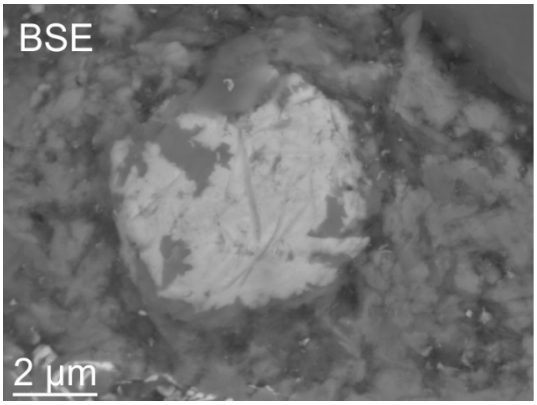

Figure 11. BSE image of a pyrite grain near the steel-clay interface, with clear evidence of alteration features.